HHS Public Access

Author manuscript

Cell Rep. Author manuscript; available in PMC 2025 May 13.

Published in final edited form as:

Cell Rep. 2025 April 22; 44(4): 115558. doi:10.1016/j.celrep.2025.115558.

Lineage-specific CDK activity dynamics characterize early mammalian development

Bechara Saykali[1], **Andy D. Tran**[2], **James A. Cornwell**[2], **Matthew A. Caldwell**[1], **Paniz Rezvan Sangsari**[3], **Nicole Y. Morgan**[3], **Michael J. Kruhlak**[2], **Steven D. Cappell**[2], **Sergio Ruiz**[1,4,*]

[1]Laboratory of Genome Integrity, Center for Cancer Research, National Cancer Institute, National Institutes of Health, Bethesda, MD, USA

[2]Laboratory of Cancer Biology and Genetics, Center for Cancer Research, National Cancer Institute, National Institutes of Health, Bethesda, MD, USA

[3]Biomedical Engineering and Physical Science Shared Resource, National Institute of Biomedical Imaging and Bioengineering, National Institutes of Health, Bethesda, MD, USA

[4]Lead contact

SUMMARY

Cyclin-dependent kinases (CDKs) regulate proliferation dynamics and cell fate in response to extracellular inputs. It remains largely unknown how CDK activity fluctuates and influences cell commitment during early mammalian development. Here, we generated a mouse model expressing a CDK translocation reporter that enabled quantification of CDK activity in live single cells. By examining pre- and post-implantation mouse embryos at different stages, we observed a progressive decrease in CDK activity in cells from the trophectoderm (TE) prior to implantation. This drop seems to correlate with the available levels of ICM-derived FGF4 as CDK activity downregulation is rescued by exogenous FGF4. Furthermore, we showed that cell fate decisions in the pre-implantation embryo are not determined by the establishment of oscillatory CDK activity or overall changes in CDK activity. Finally, we uncovered the existence of conserved regulatory mechanisms in mammals by revealing lineage-specific regulation of CDK activity in TE-like human cells.

In brief

Saykali et al. generated a mouse model that enables the quantification of CDK activity dynamics in live cells and found lineage-specific CDK regulation in cells from the pre-implantation mouse

*Correspondence: sergio.ruizmacias@nih.gov.

AUTHOR CONTRIBUTIONS

B.S. and S.R. conceived the study and performed and analyzed most of the experiments. J.A.C. and S.D.C. performed the live tracking experiments in vitro. A.D.T. and M.J.K. analyzed the confocal microscopy data. M.A.C. provided technical support. P.R.S. and N.Y.M. provided polydimethylsiloxane stamps for the gastruloid experiments. S.R. supervised the study and wrote the manuscript, with comments from all authors.

DECLARATION OF INTERESTS

The authors declare no competing interests.

SUPPLEMENTAL INFORMATION

Supplemental information can be found online at https://doi.org/10.1016/j.celrep.2025.115558.

embryo. This regulation is conserved in other mammals and seems to be dependent on the levels of ICM-derived FGF4 in mice.

Graphical Abstract

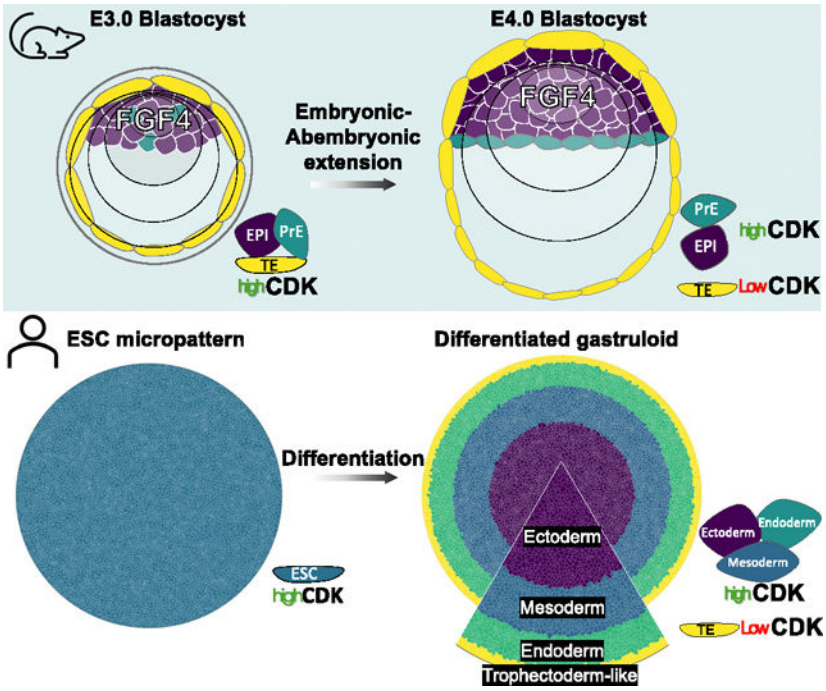

INTRODUCTION

The cell cycle is tightly controlled by complexes of cyclins and cyclin-dependent kinases (CDKs).[1] Mitogens trigger the upregulation of D-type cyclins in G1 phase, which activate CDK4 and CDK6.[2] Together with E/A-type cyclins and their associated CDKs (mainly CDK2 but also CDK1), cyclin D-CDK4/6 phosphorylate and inactivate the retinoblastoma protein RB1 leading to E2F-mediated transactivation of genes required for S phase progression.[3] At the end of G2, B-type cyclins translocate to the nucleus and activate CDK1 to promote mitotic entry. An additional layer of control is imposed by the INK4 ($p16^{Ink4a}$/$p15^{Ink4b}$/$p18^{Ink4c}$/$p19^{Ink4d}$) and CIP/KIP ($p27^{kip1}$/$p21^{cip1}$/$p57^{kip2}$) families of CDK inhibitors, which inhibit CDK4/6 or CDK1/2 complexes, respectively.[4] In summary, cell-cycle progression is controlled by oscillatory CDK activity regulated by the timely expression of cyclins and CDK inhibitors.

Embryonic development is a prime example of control over cell division dynamics to regulate cell number and fate.[5] The zygote develops into a blastocyst, a hollow sphere with an outer polarized epithelium (trophectoderm, TE) enclosing the inner cell mass (ICM).[6] Before implantation, the ICM differentiates into primitive endoderm (PrE) and the epiblast (EPI). The TE and PrE will give rise to extra-embryonic tissues, whereas the EPI will develop the fetus.[7,8] At the 8-cell (8C) stage, the first lineage decision is made based on the mutually exclusive expression of CDX2 and SOX2, which specify TE and ICM,

respectively. The second lineage decision occurs within the ICM at embryonic day 3.5 (E3.5) and involves the expression of NANOG, to specify the EPI, and GATA6 to specify the PrE.[7,8] Although the duration of the first divisions following fertilization is around 20 h, EPI cells quickly divide approximately every 10 h.[5] Moreover, polar TE cells (in contact with the ICM) proliferate more rapidly than mural TE cells (encompassing the blastocyst cavity).[9] After implantation, mural TE cells differentiate into trophoblast giant cells (TGCs), mononuclear but polyploid cells, while polar TE cells remain multipotent and highly proliferative, generating the extra-embryonic ectoderm (ExE). Finally, the EPI organizes into a rosette of polarized cells to form the egg cylinder, with cells showing extremely short doubling times (5–8 h).

Pre-implantation development is an autonomous process independent of exogenous mitogens, suggesting that cell-cycle regulatory pathways work differently in embryonic cells.[10] Indeed, RB1 is undetectable until the late blastocyst,[11] and the expression of CDK inhibitors is low or non-existent before implantation.[5,12] These observations explain the fast cell divisions and the shortened G1 and G2 phases during early development. Most of our knowledge of cell-cycle regulation in the pre-implantation embryo derives from studies on embryonic stem cells (ESCs), the *in vitro* counterpart of the ICM.[13,14] ESCs proliferate rapidly and show truncated G1 and G2 phases, recapitulating what was observed in the ICM.[13,15] They divide approximately every 10 h and show high and constitutive levels of cyclins E/A and CDK1/2 activity.[16] Moreover, although the cyclin B-CDK1 complex retains some periodical activity, it is substantially higher than in somatic cells[16] and it is needed to maintain their epigenetic identity.[17] However, it is unclear whether embryonic cells from different lineages show oscillatory or constitutive CDK regulation or whether changes in CDK activity influence cell fate decisions *in vivo*. Thus, we generated a mouse model that enabled live CDK activity quantification. While EPI cells retain elevated CDK activity, we observed a drastic reduction in TE cells prior to implantation that seems due to low fibroblast growth factor (FGF) signaling. Furthermore, we confirmed lineage-specific downregulation of CDK activity in human gastruloids, demonstrating the existence of conservation in this process.

RESULTS

Generation of a mouse model to examine CDK activity

We used a described CDK sensor,[18] including a portion of the DNA human helicase B (DHB) containing four CDK phosphorylation sites fused to mClover3. We generated a transgene encoding for both the CDK sensor and the histone 2B (H2B) fused to mRuby3 separated by a T2A self-cleaving peptide sequence (DHB/H2B hereafter; Figure 1A). As the cell progresses through the cell cycle, the fluorescent-based reporter translocates between the nucleus (low activity) and the cytoplasm (high activity) in a CDK-dependent manner, providing a quantifiable readout of CDK activity at a single-cell level (Figure 1A). We developed murine ESCs carrying our modified CDK sensor integrated at the Rosa26 locus ($ESC^{DHB/H2B}$; Figure 1A). Imaging the CDK sensor in proliferating $ESC^{DHB/H2B}$ revealed that most cells showed cytoplasmic localization and confirmed elevated CDK activity (Figures 1B and S1A). We used the cytoplasmic-to-nuclear intensity ratio (C/N) of the

DHB-mClover3 chimeric protein as a proxy to quantify CDK activity.[18] When we tracked individual ESC$^{DHB/H2B}$, we observed that following mitosis, cells maintain elevated levels of CDK activity compared to somatic cells (over a log2 C/N ratio of −1; see below) as the reporter immediately shuffled to the cytoplasm (Figures 1C and S1A). To validate the responsiveness of the CDK sensor, we treated ESC$^{DHB/H2B}$ with a CDK1/2 inhibitor (CDK1/2i) and observed efficient dose-dependent nuclear accumulation, demonstrating its excellent dynamic range (Figures 1B–1E and S1B). Furthermore, we also detected nuclear translocation following treatment with mammalian target of rapamycin (mTOR) or MYC inhibitors,[19,20] which promote a quiescent-like state in ESCs (Figures S1C and S1D).

The DHB-based sensor responds primarily to changes in CDK2 activity.[18] However, ESCs show elevated and constitutive CDK2 and CDK1 activity. Therefore, to determine their contribution, we examined DHB-mClover3 translocation dynamics by using the CDK2i PF-07104091 (hereafter, PF4091) and observed a dose-dependent inhibitory effect. However, the level of translocation is lower compared to CDK1/2i-treated ESC$^{DHB/H2B}$ (Figure S1E). CDK2-knockout ESC$^{DHB/H2B}$ showed cytoplasmic localization of the sensor, suggesting cell adaptation and the contribution of additional CDKs (Figure S1F). Consistent with previous observations on the minor role of CDK4 in ESCs,[21,22] the CDK4/6i PD-0332991 (palbociclib) in combination with PF4091 did not promote nuclear accumulation of the sensor (Figure S1G). To examine the role of CDK1, we generated CDK1 degron ESC$^{DHB/H2B}$ lines (Figures S1H and S1I). We observed that although acute CDK1 depletion did not trigger nuclear accumulation of the reporter, it showed a dose-dependent effect when combined with PF4091 (Figure 1F). Similar results were observed by using the CDK1i RO-3306 in CDK2-knockout ESC$^{DHB/H2B}$ (Figure S1J). These observations demonstrated that translocation dynamics of the CDK sensor are mainly influenced by CDK2 and CDK1 in ESCs.

We next microinjected ESC$^{DHB/H2B}$ into blastocysts to generate chimeras and established two independent mouse lines. Mouse embryonic fibroblasts (MEF$^{DHB/H2B}$) showed nuclear localization of the CDK sensor in newly born cells, correlating with low CDK activity (cells ranging a log2 C/N ratio between −2.5 and −1.5), and progressively translocates to the cytoplasm during S phase (Figures 1G, 1H, and S1K). Tracking individual MEF$^{DHB/H2B}$ showed, similar to human fibroblasts,[18] the existence of cells undergoing G1 exit as well as two populations of cells defined by their CDK activity kinetics (Figures 1G and 1H). We also examined the node, a quiescent cup-shaped structure on the ventral surface of gastrulating embryos and observed nuclear localization of the CDK sensor (Figure 1I). Collectively, we successfully generated a mouse model to analyze CDK activity.

CDK activity during pre-implantation development

To examine CDK activity during development, we collected embryos at different stages. Given that transcriptional activity slowly starts at the 2C stage, the CDK sensor was only reliably quantified from the morula stage onward (Figures 2A, S2A, and S2B). To distinguish between ICM and TE, we used SOX2 and CDX2 as markers, respectively (Figures 2A, 2B, and S2A–S2C). Embryonic cells from morula to the mid-blastocyst stage and independent of their cell lineage mainly showed cytoplasmic localization of the CDK

sensor (Figures 2A, 2B, and S2C) suggesting that elevated CDK activity drives this period of development. However, we consistently observed nuclear accumulation of the CDK reporter in CDX2$^+$ cells at the late blastocyst stage (Figures 2A, 2B, and S2C). To validate this observation, we performed time-lapse imaging in E3.5 blastocysts cultured *ex vivo* and confirmed that TE cells progressively transitioned to show nuclear localization as the embryo approaches implantation (Figure 2C; Video S1). We next quantified CDK activity in individual TE and ICM cells and observed that, while cells from the ICM showed minor oscillations in CDK activity, TE cells are more heterogeneous, with a subset of cells downregulating CDK activity (Figure 2D). We occasionally observed TE cells undergoing endoreplication, suggesting that this process occurs prior to implantation (Figure S2D).

We also examined GATA6$^+$ cells (PrE) and NANOG$^+$ cells (EPI) and observed cytoplasmic localization of the CDK sensor (Figures 2E and S2E). Fast proliferation kinetics in the PrE are needed after implantation to expand and generate the visceral endoderm (VE) and parietal endoderm. Finally, we examined post-implantation EPI from E6.5 embryos and observed cytoplasmic localization of the CDK sensor in most cells in agreement with their fast proliferation kinetics (Figure 2F). In summary, our data revealed that TE cells downregulate CDK activity prior to implantation.

FGF4-dependent regulation of CDK activity in the TE

To study the differential regulation of CDK activity between embryonic and extra-embryonic cells, we used ESC and trophoblast stem cells (TSCs), as the corresponding *in vitro* ICM and TE counterparts, respectively. TSC$^{DHB/H2B}$ showed cytoplasmic localization of the CDK sensor and responds to CDK inhibition similar to ESCs, suggesting that CDK activity downregulation in TE cells depends on non-autonomous mechanisms (Figures 3A, S3A, and S3B). Thus, we examined the response of the sensor to the deprivation of self-renewal signals. ESCs self-renew in the presence of leukemia inhibitory factor (LIF),[23] while TSCs rely on FGF4.[24] Indeed, FGF4 deprivation induces differentiation into non-proliferating TGCs following p57^{KIP2}-dependent CDK1 inhibition.[25] While LIF withdrawal in ESCs, which promotes differentiation,[26] did not induce nuclear translocation of the CDK reporter, FGF4 withdrawal resulted in most TSCs showing nuclear localization (Figure 3A). We tracked individual ESCs and TSCs to examine their behavior. ESCs showed homogeneous and robust cycling with LIF, which was maintained upon its withdrawal (Figures 3B and 3C). However, TSCs cultured with FGF4 already have a lower DHB C/N ratio compared to ESCs, including cells exiting in G1 phase (Figures 3B and 3C). FGF4-deprived TSCs showed a further drop in DHB C/N ratio with cells exiting from G1 or G2 phases, as well as cells undergoing endoreplication (Figures 3B, 3C, and S3C). Importantly, the response to FGF4 deprivation is dose dependent (Figure S3D). Finally, we observed that differentiated TSCs with nuclear CDK sensor showed increased p57^{KIP2} levels compared to ESCs (Figures S3E and S3F). In summary, TSCs were intrinsically more prone than ESCs to downregulate CDK activity upon the withdrawal of self-renewing signals.

We investigated whether the lack of FGF4 signaling *in vivo* was responsible for the drop in CDK activity. Since FGF4 is exclusively expressed by the ICM, but TE cells express both FGF receptors (FGFR1 and FGFR2),[12,27,28] the levels of FGF4 might not be enough

to sustain elevated CDK activity. We found that exogenous FGF4 prevented the nuclear accumulation of the CDK sensor in TE cells supporting the idea of an FGF4-dependent signaling gradient through the embryonic-abembryonic axis (Figures 3D and 3E; Video S2).

We next examined the peri-implantation embryo by using a protocol supporting the *in vitro* development of blastocysts beyond the implantation stages[29] (Figure 3F). We isolated E3.5–E3.75 blastocysts and imaged them. Following attachment, the polar TE expands and generates the ExE, while cells from the mural TE quickly spread and differentiated into TGCs (Figures 3G and, 3H; Video S3). TGCs showed consecutive rounds of nuclear/cytoplasmic shuttling of the CDK sensor and 5-ethynyl-2′-deoxyuridine incorporation, with no signs of mitotic events (Figures 3I and S3G; Video S3). We determined that CDK2 drives genome replication in endoreplicating TGCs, as CDK2i-treated embryos did not show the expected shuttling of the CDK sensor (Video S4). Furthermore, attached embryos also expressed $p57^{KIP2}$, which, like FGF4-deprived TSCs, might keep CDK1 inhibited to enable endoreplication (Figure 3J). Interestingly, we did not detect $p57^{KIP2}$ expression in TE cells, suggesting that implantation is required for $p57^{KIP2}$ expression *in vivo* (Figure S3H).

Embryonic cells identified by SOX2 expression showed elevated CDK activity (Figures 3G and 3H). Furthermore, polar TE cells were found adjacent to embryonic cells and showed cytoplasmic localization of the sensor (Figures 3G and 3H). We also cultured embryos into the stage of egg cylinder and observed that EPI, ExE, and VE cells still contained high levels of CDK activity to sustain the elevated rate of cell proliferation needed prior to gastrulation (Figure S3I). Our findings supported the existence of differential availability in the levels of ICM-derived FGF4, which enabled TE cells to downregulate CDK activity and prime them toward TGC differentiation.

Human TE-like cells show decreased CDK activity in a gastruloid model

We established human ESC (hESC) lines constitutively expressing the CDK sensor ($hESC^{DHB/H2B}$). Although hESCs are in a primed pluripotent state, a more advanced developmental stage compared to naive mouse ESCs, they showed elevated CDK activity (Figures 4A and S4A). Moreover, naive $hESC^{DHB/H2B}$ lines also showed similar levels of CDK activity (Figure S4B). $hESC^{DHB/H2B}$ responded to CDK1/2i as well as to acute inhibition of CDK2 (Figures S4A and S4B). Furthermore, by examining CDK2-deficient $hESC^{DHB/H2B}$ we confirmed that the CDK reporter was also regulated by CDK1 (Figure S4C).[30] Individual tracking of $hESC^{DHB/H2B}$ revealed that following mitosis, CDK activity was maintained as elevated (Figure 4B). To examine CDK activity during TE specification, we used a two-dimensional system mimicking human gastrulation.[31,32] In this system, circular-shaped micropatterned hESCs, stimulated with BMP4, differentiate into radially organized cellular rings. Starting from the outer ring of cells toward the center of the circle, cells were specified as TE, endoderm, mesoderm, and ectoderm (Figures S4D and S4E). Interestingly, we observed an enrichment in cells showing low CDK activity in the outer ring of TE-like cells (Figures 4C, S4D, and S4E). This was specific to BMP4-treated gastruloids as untreated cells neither properly differentiated nor showed nuclear accumulation of the DHB-mClover3 reporter across the gastruloid (Figure 4C). We divided the gastruloid into five circular bins and plotted the DHB-mClover3 ratio for a defined number of total cells

within the gastruloid (Figures 4D and 4E). We detected a clear accumulation of nuclear signal in the outer bin, suggesting that TE-like cells showed low levels of CDK activity (Figure 4E). Indeed, we detected a clear increase in the number of cells with nuclear CDK sensor in $CDX2^+$ cells located at the outermost part of the gastruloid (Figures 4F, 4G, and S4F). We confirmed this observation by examining $TFAP2C^+$ cells, a different marker for TE-like cells (Figures S4G and S4H). Importantly, cells expressing markers from the mesoderm or the ectoderm (Brachyury or SOX2, respectively) did not contain cells with a detectable sensor in the nucleus (Figures S4I–S4K). Finally, we examined whether human TE-like cells induced $p57^{KIP2}$ and detected enrichment in the outer ring of differentiated gastruloids (Figure 4H). In summary, these results underscored the existence of conserved CDK regulation in humans.

DISCUSSION

We revealed the existence of a dynamic and lineage-specific CDK activity landscape during early development. We showed how TE cells progressively lower CDK activity as the mouse blastocyst approaches implantation. This switch seems induced by decreased FGF4 availability and not by TE-specific autonomous mechanisms. This idea is supported by the exclusive expression of FGF4 in the ICM but the shared expression of its receptors in the EPI/TE.[27,28] Our results suggest that FGF ligands preferentially act locally and establish a CDK activity-signaling gradient. Similar observations were made in an ERK-KTR mouse model.[33,34] FGF4 signaling is required for maintaining TE identity and proliferation in TSCs, suggesting that low FGF4 signaling in the mural TE primes them to differentiate. Conversely, FGF4 signaling is required for polar TE cells to retain multipotency upon implantation.[35] In summary, FGF ligands act as positional cues to spatially and temporally pattern CDK activity in the pre-implantation embryo.

Elevated CDK activity in ESCs is associated with their pluripotency potential and self-renewal abilities.[17,36] Indeed, a lengthening in the cell-cycle duration by imposing CDK cyclic activity leads to differentiation.[37,38] Moreover, overexpression of specific CDK or cyclins facilitate somatic cell reprogramming.[39] These observations highlight the intimate link between CDK activity and cell fate. We began to detect changes in CDK activity in TE cells from E3.5 blastocysts, a stage where the blastocyst is already segregated into TE and ICM. Subsequent segregation of the ICM into EPI and PrE is characterized by the absence of clear changes in CDK activity. Thus, our results indicate that cell fate decisions during pre-implantation development are not determined by changes in CDK activity.

We also revealed conserved regulatory mechanisms in mammals during implantation. Although murine and primate embryos are morphologically similar around implantation, they show different behavior and morphogenic transformations at implantation.[40] Nevertheless, TE-like cells differentiated in gastruloids transcriptionally resemble TE cells from the E7 pre-implantation human blastocyst[31] and thus seem comparable to pre-implantation mouse TE cells.

Limitations of the study

Because we used transgenic males with wild-type females to obtain embryos and there was no maternal contribution of the reporter, we could not examine CDK activity levels in the earliest developmental stages due to low expression. It would have been of interest to correlate CDK activity with ERK activity levels in the embryo as they seem similarly regulated. In addition, the use of specific markers to discriminate TE cell subpopulations could have provided insights into a differential effect in the mural and polar TE. Finally, we show that human TE-like cells are also characterized by a drop in CDK activity. However, the role of FGF or alternative morphogens in promoting this drop was not investigated in this study.

RESOURCE AVAILABILITY

Lead contact

All requests for additional information and resources should be directed to Sergio Ruiz Macias (sergio.ruizmacias@nih.gov).

Materials availability

Reagents from this study are available upon request from the lead contact.

Data and code availability

- All data associated with the study are found in the figures and accompanying supplemental information.
- All code generated for this study is available at the Zenodo repository and is publicly available. A link to the code is listed in the key resources table.
- Any additional information required to reanalyze the data reported in this paper is available from the lead contact upon request.

STAR★METHODS

EXPERIMENTAL MODEL AND STUDY PARTICIPANT DETAILS

Cell lines and culture: Wild-type (R1, male cell line) ESC were grown on 0.1% gelatin-coated plates or alternatively on a feeder layer of growth-arrested MEF in high-glucose DMEM (11965–092, Gibco) supplemented with 15% FBS, 1:500 leukemia inhibitory factor (LIF; made in house), 0.1 mM nonessential amino acids (11140–050, Gibco), 1% glutamax (35050–61, Gibco), 55 mM β-mercaptoethanol (31350–010, Gibco) and 1% penicillin/streptomycin (15070–063, Gibco) at 37°C and 5% CO2. Cells were routinely passaged with Trypsin 0.05% (25300–054, Gibco). Media were changed every other day and passaged every 2–3 days. MEF were grown in DMEM, 10% FBS, and 1% penicillin/streptomycin. HEK293T (a gift from Dr. Inder Verma, SALK Institute, San Diego, CA, USA) cells were grown in DMEM, 10% FBS, and 1% penicillin/streptomycin. Generation of infective lentiviral particles and ESC infections were performed as described (Ruiz et al., 2011).

To generate ESC$^{DHB/H2B}$ lines, we first made a targeting construct using CRE-treated and BstBI/MluI digested LSL-Cas9-ROSA26TV plasmid donor (gift from Feng Zhang, #61408, Addgene) to subclone the DHB-mClover3_2A_H2B-mRuby3 fragment. This fragment was generated by Gibson assembly (New England Biolabs) using synthetized gene fragments (IDT technologies). To generate CDK1$^{FKBP/FKBP}$ ESC lines, we followed a similar approach. Fragments to generate the recombination construct (2xHA-FKBP-2A-TagBFP, see primers in Table S1) were amplified by PCR and ligated them by Gibson cloning using the plasmid backbone from CTCF-mAC donor (gift from Masato Kanemaki, #140646, Addgene). ESC were co-transfected using jetPRIME (PolyPlus transfection) with the targeting vector as well as with LentiCRISPRv2 (gift from Feng Zhang, #52961, Addgene) encoding a sgRNA designed to target the ROSA26 or CDK1. Targeting events are uncommon and therefore, mClover3+ or TagBFP ESC were sorted on a BD FACSAria Fusion instrument.

Trophoblast stem cells (TSC, unknown sex of the cell line) (gift from Magdalena Zernicka-Goetz, Caltech) were cultured on an irradiated layer of MEF in RPMI-1640 medium supplemented with 20% FBS, Glutamax (1x, Gibco), 0.1 mM nonessential amino acids (1x, Gibco), Sodium pyruvate (1x, Gibco), 55 mM 2-Mercaptoethanol (100 μM, Gibco), 1% penicillin/streptomycin (Gibco), FGF4 (25 ng/mL), and heparin (1 μg/mL). To generate TSC$^{DHB/H2B}$ lines, we first generated a lentiviral vector to constitutively express the transgene DHB-mClover3_2A_H2B-mRuby3 by cloning this fragment into BamHI/EcoRI digested FUGW (Gift from David Baltimore, #14883, Addgene). TSC were trypsinized and infected in suspension with infective lentiviral particles. Infected clonal TSC lines were established and amplified in culture.

Human ESC (hESC, H9 cell line, female cell line, Wicell Institute) were cultured in wells coated with growth factor reduced Matrigel (354230, Corning) in mTeSR plus medium (Stemcell, #100–0276) with daily changes of media. Cells were passaged at 80% confluency using 1 mg/mL Dispase (Stemcell, #07923) and manual scrapping and cultured at 37°C and 5% CO2. To generate hESC$^{DHB/H2B}$ lines, H9 cells were trypsinized and infected in suspension with infective lentiviral particles. Infected clonal hESC lines were established and amplified in culture. To reprogram primed H9 cells into a naive state we used RSeT medium (Stem Cell Technologies) following manufacturer's instructions. All experiments conducted with hESC followed protocols approved by the National Institutes of Health ESCRO committee and are in compliance with the principles laid out in the ISSCR 2021 guidelines (all experiments from this work fall under the Category 1).

For the experiments performed with the cell lines used in this study, sex was not considered as a variable and should not be considered as a limitation for the conclusions of this work. None of the cell lines used in this manuscript are listed in the International Cell Line Authentication Committee (ICLAC) Database of Cross-contaminated or Misidentified Cell Lines and have not been authenticated. Testing for mycoplasma contamination in our cells was performed routinely. No sample size was calculated. All experiments were performed at least two independent times with two to three technical replicates in at least two independent mouse and human ESC clonal lines. The number of replicates, independent mouse and human ESC clones and experiments are standard in the field.

Mice: All mouse breeding and experimentation followed protocols approved by the National Institutes of Health Institutional Animal Care & Use Committee (ACUC, protocol 07–37) Guideline for Breeding and Weaning. C57BL/6J mice obtained from the Jackson Laboratory, Bar Harbor, ME. Mice were maintained in a dark/light cycle of 12 h each in a temperature range of 68°−76°F and a range of 30–70% humidity. To generate the ROSA26$^{DHB/H2B}$ mice, we microinjected ESC$^{DHB/H2B}$ into C57BL/6 blastocysts and transferred to pseudo-pregnant females. Several ROSA26$^{DHB/H2B}$ mouse chimeras were generated from which we established two mouse lines. The two independent ROSA26DHB$^{/H2B}$ mouse lines generated were functionally comparable although all experiments shown in this manuscript correspond to one of these lines. ROSA26$^{DHB/H2B}$ mice were generated by the Mouse Modeling & Cryopreservation (MMC) facility at the National Institutes of Health (NIH). To genotype, genomic DNA was extracted from a small ear biopsy and PCR was performed with GoTaq Hot Start Polymerase (Promega) using specific primers (see primers in Table S1). All experiments were done in pre- or post-implantation mouse embryos and the sex of the embryos was not considered as a variable and should not be considered as a limitation for the conclusions of this work.

METHOD DETAILS

Mouse embryonic fibroblast isolation: Mouse embryos from pregnant females were collected at E13.5. The head and organs from the embryos were removed in PBS and thereafter transferred into a clean dish. Embryos were finely minced in minimal amount of carry over PBS and incubated for 15 min at 37C with 1mL of 0.05% trypsin/EDTA. Cells were dissociated by energic pipetting up and down. Trypsin was then inactivated in DMEM containing 10% FBS and 0.1 mM nonessential amino acids (Gibco). Cells from an individual embryo were centrifuged, plated in a p100 plate and routinely passaged every 3–4 days.

Embryo collection and culture: For embryo collection, male heterozygous ROSA26$^{DHB/H2B}$ mice were mated with four to six weeks old female wild-type mice. Females were intraperitoneally injected with 5 IU of pregnant mare serum gonadotropin (PMSG, Prospec), followed 48 h later by 5 IU of human chorionic gonadotropin (hCG; Sigma-Aldrich). Alternatively, eight-weeks-old naturally pregnant females were also used for embryo isolation. Pre-implantation embryos (zygotes, 2C, 4C-stage embryos, morulas and blastocysts of different age) were flushed from the oviducts and collected in M2 media (MR-015-D, Sigma-Aldrich) while post-implantation embryos (E5.5 and E7.5) were collected in DMEM/F-12 (Gibco) supplemented with 10% FBS, 15 mM HEPES, 1% Penicillin-Streptomycin and 1X L-glutamine. For time-lapse microscopy experiments performed with isolated E3.5 hemizygous ROSA26$^{DHB/H2B}$ embryos we first digested the zona pellucida with Tyrode's acid, washed three times in M2 and then transferred to IVC1 medium (DMEM/F12 supplemented with 20% (vol/vol) heat-inactivated FBS, 2 mM L-glutamine, penicillin/streptomycin (25 μg/mL), 13 ITS-X (10 mg per liter insulin, 5.5 mg per liter transferrin, 0.0067 mg per liter sodium selenite and 2 mg per liter ethanolamine), 8 nM β-estradiol, 200 ng/mL progesterone and 25 μM *N*-acetyl-L-cysteine) for up to 48 h in 18-wells chambered coverslips (Ibidi). Following attachment and spread, embryos were switched and further cultured in IVC2 (DMEM/F12 supplemented with 30% (vol/vol) KSR,

2 mM L-glutamine, penicillin (25 units/ml)/streptomycin (25 μg/mL), 13 ITS-X (10 mg per liter insulin, 5.5 mg per liter transferrin, 0.0067 mg per liter sodium selenite and 2 mg per liter ethanolamine), 8 nM β-estradiol, 200 ng/mL progesterone and 25 μM *N*-acetyl-L-cysteine), as described. Experiments performed in E3.5 ROSA26$^{DHB/H2B}$ embryos with the addition of exogenous FGF4 (1 μg/mL) were performed in uncoated 18-wells chambered coverslips (Ibidi) to prevent attachment. To quantify the translocation levels of the CDK sensor during development, two independent datasets with embryos at different stages of development were collected (Figure 2C, *N* = 54; Figure S3C, N = 46).

RNA extraction and qPCR: Isolation of total RNA was performed by using the Isolate II RNA Mini Kit (Bioline) followed by cDNA synthesis (SensiFAST cDNA Synthesis Kit, Bioline). Quantitative real-time PCR was performed with PowerUp SYBR Master mix in a QuantStudio 6 Pro system (see primers in Table S1). When analyzing quantitative real-time PCR data, we considered statistically significant those samples that when compared showed an averaged of 2-fold difference in overall gene expression and an unpaired two-tail t test with a *p*-value of at least 0.05 or lower. Three independent experiments including at least two independent clonal cell lines were performed but only one is shown in the figures.

Immunofluorescence: Mouse and human ESC$^{DHB/H2B}$ were fixed in 2% paraformaldehyde (Electron Microscopy Sciences) for 10 min at room temperature and permeabilized for 10 min using the following permeabilization buffer (100mM Tris-HCl pH 7.4, 50mM EDTA pH 8.0, 0.5% Triton X-100). Embryos were fixed in 4% paraformaldehyde for 10 min, permeabilized for 30 min in 0.3% Triton X-100 and 0.1 M glycine in 13 phosphate-buffered saline (PBS) and blocked for 1 h with 1% bovine serum albumin (BSA) and 0.1% Tween in 1× PBS. ESC and embryos were incubated overnight with primary antibodies, washed in 0.1% Tween in 1× PBS, and incubated with the secondary antibody accordingly for 1 h at room temperature. For EdU staining, embryos were incubated with 10mM EdU (Click Chemistry Tools) for 30 min before fixation. EdU incorporation was visualized using Alexa Fluor 647-azide (Click Chemistry Tools) Click-IT labeling chemistry and Copper protectant to preserve the fluorescence signal from the CDK sensor. Images were acquired using the Nikon SoRa spinning disk confocal microscope equipped with 20x plan-apochromat, 40x plan-apochromat lD 40x OFN25 DIC N2 Air and 60x apochromat TIRF Oil DIC N2 objective lenses (N.A. 0.75, 0.95 and 1.49, respectively) or a Zeiss LSM880 confocal microscope equipped with 20x plan-apochromat and 40x plan-apochromat Oil (N.A. 0.8 and 1.3, respectively) and stage top incubators to maintain temperature, humidity and CO2 concentration (Tokai Hit STX and Okolab Bold Line, respectively). For time-lapse microscopy experiments with embryos, images were acquired every 20 min. Image processing was done using Nikon's NIS-Elements software (v.5.4.1) and images were denoised using the denoise.ai module.

High throughput imaging (HTI): A total of 10,000–20,000 human or mouse ESC$^{DHB/H2B}$ (depending on the experiment and on the specific ESC line) were plated on gelatinized μCLEAR bottom 96-well plates (Greiner Bio-One, 655087). ESC were treated with CDK1/2i (different concentrations in the range from 1 to 30μM depending on the experiment), CDK2i (PF4091 (2 μM–20μM) or CVT313 (200nM–30μM)), CDK1i

(RO-3306, 200nM–10μM), Palbociclib (0.2μM–5μM), MYCi (25μM–200μM), mTORi (75nM–500nM) and dTAG (500nM) for one to 2 h depending on the experiment before fixation with 4% PFA in PBS for 10 min at room temperature. Images were automatically acquired using a CellVoyager CV7000 high throughput spinning disk confocal microscope (Yokogawa, Japan). Each condition was always performed in triplicate wells and at least 9 different fields of view (FOV) were acquired per well. All experiments were performed at least three times with two independent ESC, TSC or hESC clonal lines. Image analysis was performed using the Signals Image Artist system (Revvity Signals). Nuclei were segmented based on H2B-mRuby3. Various measurements were calculated over the nuclear masks, including mean fluorescence intensities from nuclei and external ring around the nuclei. Cell-level data was exported as text files, then analyzed and plotted using R version 4.3.1.

Western blot: Cells were trypsinized and lysed in 50 mM Tris pH 8, 8 M Urea (Sigma) and 1% Chaps (Millipore) followed by 30 min of shaking at 4°C. A total of 20 μg of extracts were run on 4%–12% NuPage Bis-Tris Gel (Invitrogen) and transferred onto Nitrocellulose Blotting Membrane (GE Healthcare). Transferred membranes were incubated with the following primary antibodies overnight at 4°C. The next day the membranes were incubated with HRP-conjugated secondary antibodies Goat anti-Rabbit IgG (H + L) (1:5000; Thermo Fisher Scientific, Cat# 31466) or Goat anti-Mouse IgG (H + L) (1:5000; Thermo Fisher Scientific, Cat# 31431) for 1 h at room temperature. Membranes were developed using SuperSignal West Pico PLUS or SuperSignal West Femto Maximum sensitivity (Thermo Scientific). For westerns, two independent experiments were performed but only one representative is shown in the figures.

Master mold Fabrication: The master mold was made from SU-8 photoresist patterned on silicon using standard photolithographic techniques. Briefly, a 4″ silicon wafer was dehydrated at 200°C for 20 min. To pattern the features, SU-8 2050 (Kayaku Advanced Materials) was spin-coated (Laurell Technologies) on the wafer for a desired height of 37 μm. The wafer was baked at 65°C for 1 min and then at 95°C for 6 min before being exposed with collimated near-UV light through a glass-chrome mask (Front Range Photomask) using a contact mask aligner (OAI Instruments) to form arrays of 1 mm diameter pillars. After exposure, the wafer was again baked at 65°C for 1 min and then at 95°C for 6 min. The unexposed areas of resist were then removed by immersing the wafer in a bath of SU-8 developer (Kayaku Advanced Materials) with gentle agitation for 6 min, followed by rinses in isopropanol and then ultrapure water. To increase durability, the master mold was hard baked at 200°C for 4 min and then cooled to room temperature at a rate of 150 °C/h. The wafer was then silanized by exposure to tridecafluoro-1,1,2,2-tetrahydrooctyl-1-trichlorosilane (UCT Specialties) vapor overnight to facilitate the unmolding steps. We decided to use a mold of SU-8 pillars followed by an additional PDMS molding step to get PDMS pillars rather than patterning SU-8 wells for two reasons: to avoid adhesion issues arising from in thermal expansion coefficient mismatches when large areas of SU-8 are in contact with the silicon, and to ensure that the pillar edges were sharp and well-defined.

Fabricating PDMS stamps: Polydimethylsiloxane/PDMS (Sylgard 184, Dow Corning) base and curing agent were mixed in a 10:1 (w:w) ratio in a planetary mixer (Thinky). 45 g of pre-mixed PDMS was then poured onto the master mold in a 100 mm Petri dish, degassed, and cured at 80°C for 1 h on a leveled shelf. The cured PDMS, with an array of wells, was then unmolded and cut. This PDMS layer was treated with oxygen plasma (Plasma Etch) for 45 s and then silanized as described above before being used as a mold for the final PDMS stamps.

PDMS base and curing agent were mixed in a 10:1 (w:w) ratio. 90 g and 70 g of pre-mixed PDMS was poured onto the PDMS mold and into an empty 100 mm Petri dish respectively. Both dishes were then degassed and cured as previously described. The plain PDMS sheet served as a backing for the PDMS pillar stamps, with the two layers bonded together after exposure to oxygen plasma for 45 s to achieve a total PDMS stamp height of 1–1.5 cm. The additional PDMS height provided ease of handling and sufficient force during the stamping process; we formed the stamp in two layers because it was convenient to use standard height petri dishes while curing the PDMS. PDMS stamps were then cut into individual pieces, approximately 6.5 mm × 6.5 mm and allowed to regain their hydrophobicity for a few days before proceeding to the next steps.

Gastruloid cell seeding protocol: H9 hESC were seeded and differentiated to generate gastruloids as described. Briefly, single-use PDMS stamps, each with an array of 3 × 3 1mm-diameter pillars, with 1 mm diameter pillars (total of 9 per well) were covered with drops of Matrigel diluted in DMEM-F12 and incubated for 30 min at 37°C. This suspension was then aspirated off and the stamps were left to dry at room temperature for up to 30 min. Matrigel-coated PDMS stamps were then brought into contact with 8-well Ibidi culture slides for 2 min. The printed surface was then washed with DMEM-F12, and wells were ready for cell seeding. Exponentially growing H9 cells at 60–80% confluency were collected by Accutase (Gibco, #A11105–01), washed with 10mL of DMEM-F12 and centrifuged at 1000rpm for 5 min. Cells were resuspended in mTeSR Plus containing 10μM Rho-associated kinase inhibitor (ROCKi, Selleckchem, #S1049) and seeded in a single eight-well chamber slide with a total number of 150,000–200,000 cells (Ibidi, #80826). Cells were incubated for 6 h at 37°C and 5% CO2, washed gently three times with warm DMEM-F12 and refed with mTeSR without ROCKi for 2 h followed with mTeSR containing 50 ng/ml BMP4 (R&D systems, #314-BP-010) for 42–48 h. At least two independent experiments with multiple gastruloids per experiment were performed but only one representative is shown in the figures.

Single cell live tracking: For all experiments the cells were plated in 96-well optical-grade plastic dishes (Ibidi) at 5000–10,000 cells per well with 300uL media per well. Images were acquired every 12 min using a Nikon Ti2-E inverted fluorescent microscope with an automated state and environmental chamber which maintained the cells at 37C and supplied with 5% CO2. Images were acquired in RFP and YFP channels with a 20×0.45 numerical aperture objective. A total of 6 regions of interest (ROIs) per well and a total of 48 wells were imaged for a period of 72 h. The total light exposure was less than 500ms for each site that was imaged. Downstream image processing, segmentation, quantification

of fluorescent signals (H2B-mRuby3 intensity and CDK-mClover3 activity), and single-cell tracking was performed using custom-written MATLAB scripts as previously described (https://github.com/scappell/Cell_tracking).

Analysis of single cell tracking data: Single cell traces were aligned to the start of the track for individual cells. CDK activity and nuclear area were quantified as previously described.[41] Combined single cell traces were aligned to the time of mitosis for each individual cells and cell fates were quantified as follows: CDK increasing (CDK inc) cells are defined as CDK activity > −0.74 within 4hrs of mitosis. CDK delayed (CDK del) cells are defined as CDK < −0.74 for the first 4hrs following mitosis and then subsequent CDK activity > −0.74. G1 exit is defined as CDK < −0.74 for the duration of the observation period. G2 exit is defined as a CDK > −0.74 after mitosis, followed by CDK < −0.74 for the remainder of the observation period. Endoreduplication is defined as exit from G2 (CDK < −0.74) followed by re-accumulation of CDK2 activity, without mitosis.

Image analysis for mouse embryos: Image analysis and segmentation was performed using custom scripts written in Python (v. 3.10). Deep learning segmentation models were trained and deployed using the NIH HPC Biowulf cluster (http://hpc.nih.gov). H2B-mRuby3 labeled embryonic nuclei were segmented using a custom trained Cellpose model,[42] creating individual nuclear ROIs. To create the cytoplasmic ROI, each nuclear label was expanded by 2 pixels and 12 pixels. The 2-pixel expansion was subtracted from the 12-pixel expansion, resulting in a cytoplasmic ROI, matched to a parental nuclear ROI. Both the nuclear and cytoplasmic ROIs were used to quantify fluorescent intensities across the other imaged markers (DHB-mClover3, CDX2 or SOX2). DHB-mClover3 cytoplasmic and nuclear intensities were used to calculate a cytoplasmic/nuclear ratio. Embryonic cells were classified as either CDX2 or SOX2 positive or negative by setting a fluorescent intensity threshold based on the distribution of nuclear marker intensities. All cells were linked to their parent embryo, allowing a cell count per embryo.

Live embryo image analysis: H2B-mRuby3 nuclei from live embryo timelapses were segmented in Imaris Bitplane (v. 10.2.0, Oxford Instruments) using the Surfaces module and then tracked using the Lineage tracking algorithm. SOX2 positive and CDX2 positive tracks were identified by comparing the final timepoint to an image of the fixed embryo stained with the appropriate markers. Cytoplasmic ROIs were created from labeled nuclei using a custom script written in Python (v. 3.10), using the method as described above. Cytoplasmic ROIs were linked to a nuclear ROI and each nucleus was tracked over time. Nuclear and cytoplasmic ROIs were used to quantify DHB-mClover3 intensity in the embryo timelapses.

Image analysis for human gastruloids: Gastruloid image analysis and segmentation was performed using custom scripts written in Python (v. 3.10). Deep learning segmentation models were trained and deployed using the NIH HPC Biowulf cluster (http://hpc.nih.gov). H2B-mRuby3 labeled gastruloid nuclei were segmented using a custom trained Cellpose model, creating individual nuclear ROIs. Cytoplasmic ROIs were generated as described for embryos, by extending the nuclear labels by 12-pixels and subtracting the nuclear + 2-pixel label. Cytoplasmic and nuclear ROIs were used to quantify marker intensities as described

above. The entire gastruloid was also segmented in order to identify the gastruloid centroid. The position of every nucleus relative to the gastruloid centroid was calculated using a Euclidean distance transform. Nuclear distances were either binned into 5 concentric rings every 100 μm away from the centroid (A = 0–100 μm, B = 100–200 μm, C = 200–300 μm, D = 300–400 μm, E ≥ 400 μm) or nuclear distances were normalized into radial distances (0–1) by calculating nuclear distance from centroid/maximum gastruloid radial distance. Cells were classified into CDX2, SOX2, TFAP2C, and BRA positive or negative by setting a fluorescent intensity threshold based on the distribution of nuclear marker intensities.

QUANTIFICATION AND STATISTICAL ANALYSIS

When analyzing HTI data, we considered statistically significant those samples that when compared showed an unpaired two-tail t test with a *p*-value of at least 0.05 or lower and an averaged Log2 fold change difference of 0.2. For all HTI experiments, three independent experiments including at least two independent clonal cell lines were performed but only one representative experiment is shown in the figures. Statistical analyses (*p*-values) from data obtained in embryos or gastruloids (Figures 2E, 3E, 4F, S4H–S4J and S4K) or derived from real-time PCR analyses (Figure S3E) were obtained from unpaired two-tailed t-tests. No sample size was calculated. All experiments with cell lines were performed at least two independent times with two to three technical replicates in at least two independent mouse and human ESC clonal lines. These number of replicates, independent mouse and human ESC clones and experiments are standard in the field.

Supplementary Material

Refer to Web version on PubMed Central for supplementary material.

ACKNOWLEDGMENTS

We thank Dr. David Santamaria, Dr. Carmen J. Williams, and members from the Laboratory of Genome Integrity for the helpful comments on this work. We also thank Dr. Ferenc Livak, Dr. Shafi Siddiqui, and the Center for Cancer Research Flow Cytometry Core; Dr. Gianluca Pegoraro and the High-Throughput Imaging Facility; and the Microscopy Core at the National Cancer Institute. The Ruiz laboratory is supported by the Intramural Research Program of the NIH, USA (project ZIA BC 011809).

REFERENCES

1. Malumbres M, and Barbacid M (2009). Cell cycle, CDKs and cancer: a changing paradigm. Nat. Rev. Cancer 9, 153–166. 10.1038/nrc2602. [PubMed: 19238148]
2. Massague J (2004). G1 cell-cycle control and cancer. Nature 432, 298–306. 10.1038/nature03094. [PubMed: 15549091]
3. Fischer M, Schade AE, Branigan TB, Müller GA, and DeCaprio JA (2022). Coordinating gene expression during the cell cycle. Trends Biochem. Sci. 47, 1009–1022. 10.1016/j.tibs.2022.06.007. [PubMed: 35835684]
4. Nakayama K, and Nakayama K (1998). Cip/Kip cyclin-dependent kinase inhibitors: brakes of the cell cycle engine during development. Bioessays 20, 1020–1029. 10.1002/(SICI)1521-1878(199812)20:12<1020::AID-BIES8>3.0.CO;2-D. [PubMed: 10048302]
5. Ciemerych MA, and Sicinski P (2005). Cell cycle in mouse development. Oncogene 24, 2877–2898. 10.1038/sj.onc.1208608. [PubMed: 15838522]
6. Yao C, Zhang W, and Shuai L (2019). The first cell fate decision in pre-implantation mouse embryos. Cell Regen. 8, 51–57. 10.1016/j.cr.2019.10.001. [PubMed: 31844518]

7. Chazaud C, and Yamanaka Y (2016). Lineage specification in the mouse preimplantation embryo. Development 143, 1063–1074. 10.1242/dev.128314. [PubMed: 27048685]
8. Rossant J (2018). Genetic Control of Early Cell Lineages in the Mammalian Embryo. Annu. Rev. Genet. 52, 185–201. 10.1146/annurev-genet-120116-024544. [PubMed: 30183407]
9. Copp AJ (1978). Interaction between inner cell mass and trophectoderm of the mouse blastocyst. I. A study of cellular proliferation. J. Embryol. Exp. Morphol. 48, 109–125. [PubMed: 744943]
10. Stewart CL, and Cullinan EB (1997). Preimplantation development of the mammalian embryo and its regulation by growth factors. Dev. Genet. 21, 91–101. 10.1002/(SICI)1520-6408(1997)21:1<91::AID-DVG11>3.0.CO;2-D. [PubMed: 9291585]
11. Iwamori N, Naito K, Sugiura K, and Tojo H (2002). Preimplantation-embryo-specific cell cycle regulation is attributed to the low expression level of retinoblastoma protein. FEBS Lett. 526, 119–123. 10.1016/S0014-5793(02)03121-6. [PubMed: 12208517]
12. Boroviak T, Loos R, Lombard P, Okahara J, Behr R, Sasaki E, Nichols J, Smith A, and Bertone P (2015). Lineage-specific profiling delineates the emergence and progression of naive pluripotency in mammalian embryogenesis. Dev. Cell 35, 366–382. 10.1016/j.devcel.2015.10.01. [PubMed: 26555056]
13. White J, and Dalton S (2005). Cell cycle control of embryonic stem cells. Stem Cell Rev. 1, 131–138. 10.1385/SCR:1:2:131. [PubMed: 17142847]
14. Padgett J, and Santos SDM (2020). From clocks to dominoes: lessons on cell cycle remodeling from embryonic stem cells. FEBS Lett. 594, 2031–2045. 10.1002/1873-3468.13862.
15. Liu L, Michowski W, Kolodziejczyk A, and Sicinski P (2019). The cell cycle in stem cell proliferation, pluripotency and differentiation. Nat. Cell Biol. 21, 1060–1067. 10.1038/s41556-019-0384-4. [PubMed: 31481793]
16. Stead E, White J, Faast R, Conn S, Goldstone S, Rathjen J, Dhingra U, Rathjen P, Walker D, and Dalton S (2002). Pluripotent cell division cycles are driven by ectopic Cdk2, cyclin A/E and E2F activities. Oncogene 21, 8320–8333. 10.1038/sj.onc.1206015. [PubMed: 12447695]
17. Michowski W, Chick JM, Chu C, Kolodziejczyk A, Wang Y, Suski JM, Abraham B, Anders L, Day D, Dunkl LM, et al. (2020). Cdk1 Controls Global Epigenetic Landscape in Embryonic Stem Cells. Mol. Cell 78, 459–476. 10.1016/j.molcel.2020.03.010. [PubMed: 32240602]
18. Spencer SL, Cappell SD, Tsai FC, Overton KW, Wang CL, and Meyer T (2013). The proliferation-quiescence decision is controlled by a bifurcation in CDK2 activity at mitotic exit. Cell 155, 369–383. 10.1016/j.cell.2013.08.062. [PubMed: 24075009]
19. Bulut-Karslioglu A, Biechele S, Jin H, Macrae TA, Hejna M, Gertsenstein M, Song JS, and Ramalho-Santos M (2016). Inhibition of mTOR induces a paused pluripotent state. Nature 540, 119–123. 10.1038/nature20578. [PubMed: 27880763]
20. Scognamiglio R, Cabezas-Wallscheid N, Their MC, Altamura S, Reyes A, Prendergast ÁM, Baumgärtner D, Carnevalli LS, Atzberger A, Haas S, et al. (2016). Myc Depletion Induces a Pluripotent Dormant State Mimicking Diapause. Cell 164, 668–680. 10.1016/j.cell.2015.12.033. [PubMed: 26871632]
21. Savatier P, Lapillonne H, van Grunsven LA, Rudkin BB, and Samarut J (1996). Withdrawal of differentiation inhibitory activity/leukemia inhibitory factor up-regulates D-type cyclins and cyclin-dependent kinase inhibitors in mouse embryonic stem cells. Oncogene 12, 309–322. [PubMed: 8570208]
22. Liu L, Michowski W, Inuzuka H, Shimizu K, Nihira NT, Chick JM, Li N, Geng Y, Meng AY, Ordureau A, et al. (2017). G1 cyclins link proliferation, pluripotency and differentiation of embryonic stem cells. Nat. Cell Biol. 19, 177–188. 10.1038/ncb3474. [PubMed: 28192421]
23. Williams RL, Hilton DJ, Pease S, Willson TA, Stewart CL, Gearing DP, Wagner EF, Metcalf D, Nicola NA, and Gough NM (1988). Myeloid leukemia inhibitory factor maintains the developmental potential of embryonic stem cells. Nature 336, 684–687. 10.1038/336684a0. [PubMed: 3143916]
24. Tanaka S, Kunath T, Hadjantonakis AK, Nagy A, and Rossant J (1998). Promotion of trophoblast stem cell proliferation by FGF4. Science 282, 2072–2075. 10.1126/science.282.5396.2072. [PubMed: 9851926]

25. Ullah Z, Kohn MJ, Yagi R, Vassilev LT, and DePamphilis ML (2008). Differentiation of trophoblast stem cells into giant cells is triggered by p57/Kip2 inhibition of CDK1 activity. Genes Dev. 22, 3024–3036. 10.1101/gad.1718108. [PubMed: 18981479]
26. Kalkan T, Olova N, Roode M, Mulas C, Lee HJ, Nett I, Marks H, Walker R, Stunnenberg HG, Lilley KS, et al. (2017). Tracking the embryonic stem cell transition from ground state pluripotency. Development 144, 1221–1234. 10.1242/dev.142711. [PubMed: 28174249]
27. Kang M, Garg V, and Hadjantonakis AK (2017). Lineage Establishment and Progression within the Inner Cell Mass of the Mouse Blastocyst Requires FGFR1 and FGFR2. Dev. Cell 41, 496–510. 10.1016/j.devcel.2017.05.003. [PubMed: 28552559]
28. Molotkov A, Mazot P, Brewer JR, Cinalli RM, and Soriano P (2017). Distinct Requirements for FGFR1 and FGFR2 in Primitive Endoderm Development and Exit from Pluripotency. Dev. Cell 41, 511–526. 10.1016/j.devcel.2017.05.004. [PubMed: 28552557]
29. Bedzhov I, Leung CY, Bialecka M, and Zernicka-Goetz M (2014). *In vitro* culture of mouse blastocysts beyond the implantation stages. Nat. Protoc. 9, 2732–2739. 10.1038/nprot.2014.186. [PubMed: 25356584]
30. Aleem E, Kiyokawa H, and Kaldis P (2005). Cdc2-cyclin E complexes regulate the G1/S phase transition. Nat. Cell Biol. 7, 831–836. 10.1038/ncb1284. [PubMed: 16007079]
31. Warmflash A, Sorre B, Etoc F, Siggia ED, and Brivanlou AH (2014). A method to recapitulate early embryonic spatial patterning in human embryonic stem cells. Nat. Methods 11, 847–854. 10.1038/nmeth.3016. [PubMed: 24973948]
32. Minn KT, Fu YC, He S, Dietmann S, George SC, Anastasio MA, Morris SA, and Solnica-Krezel L (2020). High-resolution transcriptional and morphogenetic profiling of cells from micropatterned human ESC gastruloid cultures. Elife 9, e59445. 10.7554/eLife.59445. [PubMed: 33206048]
33. Simon CS, Rahman S, Raina D, Schröter C, and Hadjantonakis AK (2020). Live Visualization of ERK Activity in the Mouse Blastocyst Reveals Lineage-Specific Signaling Dynamics. Dev. Cell 55, 341–353. 10.1016/j.devcel.2020.09.030. [PubMed: 33091370]
34. Pokrass MJ, Ryan KA, Xin T, Pielstick B, Timp W, Greco V, and Regot S (2020). Cell-Cycle-Dependent ERK Signaling Dynamics Direct Fate Specification in the Mammalian Preimplantation Embryo. Dev. Cell 55, 328–340. 10.1016/j.devcel.2020.09.013. [PubMed: 33091369]
35. Christodoulou N, Weberling A, Strathdee D, Anderson KI, Timpson P, and Zernicka-Goetz M (2019). Morphogenesis of extra-embryonic tissues directs the remodeling of the mouse embryo at implantation. Nat. Commun. 10, 3557. 10.1038/s41467-019-11482-5. [PubMed: 31391456]
36. Wang XQ, Lo CM, Chen L, Ngan ES, Xu A, and Poon RY (2017). CDK1-PDK1-PI3K/Akt signaling pathway regulates embryonic and induced pluripotency. Cell Death Differ. 24, 38–48. 10.1038/cdd.2016.84. [PubMed: 27636107]
37. Pauklin S, and Vallier L (2013). The cell-cycle state of stem cells determines cell fate propensity. Cell 155, 135–147. 10.1016/j.cell.2014.02.044. [PubMed: 24074866]
38. White J, Stead E, Faast R, Conn S, Cartwright P, and Dalton S (2005). Developmental activation of the Rb-E2F pathway and establishment of cell cycle-regulated cyclin-dependent kinase activity during embryonic stem cell differentiation. Mol. Biol. Cell 16, 2018–2027. 10.1091/mbc.e04-12-1056. [PubMed: 15703208]
39. Ruiz S, Panopoulos AD, Herrerıás A, Bissig KD, Lutz M, Berggren WT, Verma IM, and Izpisua Belmonte JC (2011). A high proliferation rate is required for cell reprogramming and maintenance of human embryonic stem cell identity. Curr. Biol. 2, 45–52. 10.1016/j.cub.2010.11.049.
40. Shahbazi MN, and Zernicka-Goetz M (2018). Deconstructing and reconstructing the mouse and human early embryo. Nat. Cell Biol. 20, 878–887. 10.1038/s41556-018-0144-x. [PubMed: 30038253]
41. Cappell SD, Chung M, Jaimovich A, Spencer SL, and Meyer T (2016). Irreversible APC(Cdh1) Inactivation Underlies the Point of No Return for Cell-Cycle Entry. Cell 166, 167–180. 10.1016/j.cell.2016.05.077. [PubMed: 27368103]
42. Pachitariu M, and Stringer C (2022). Cellpose 2.0: how to train your own model. Nat. Methods 19, 1634–1641. 10.1038/s41592-022-01663-4. [PubMed: 36344832]

Highlights

- Translocation of a CDK reporter in pluripotent ESC is regulated by CDK1 and CDK2
- Cells from the trophectoderm show a decrease in CDK activity prior to implantation
- CDK activity downregulation is rescued by exogenous FGF4
- Lineage-specific CDK regulation is conserved in other mammals

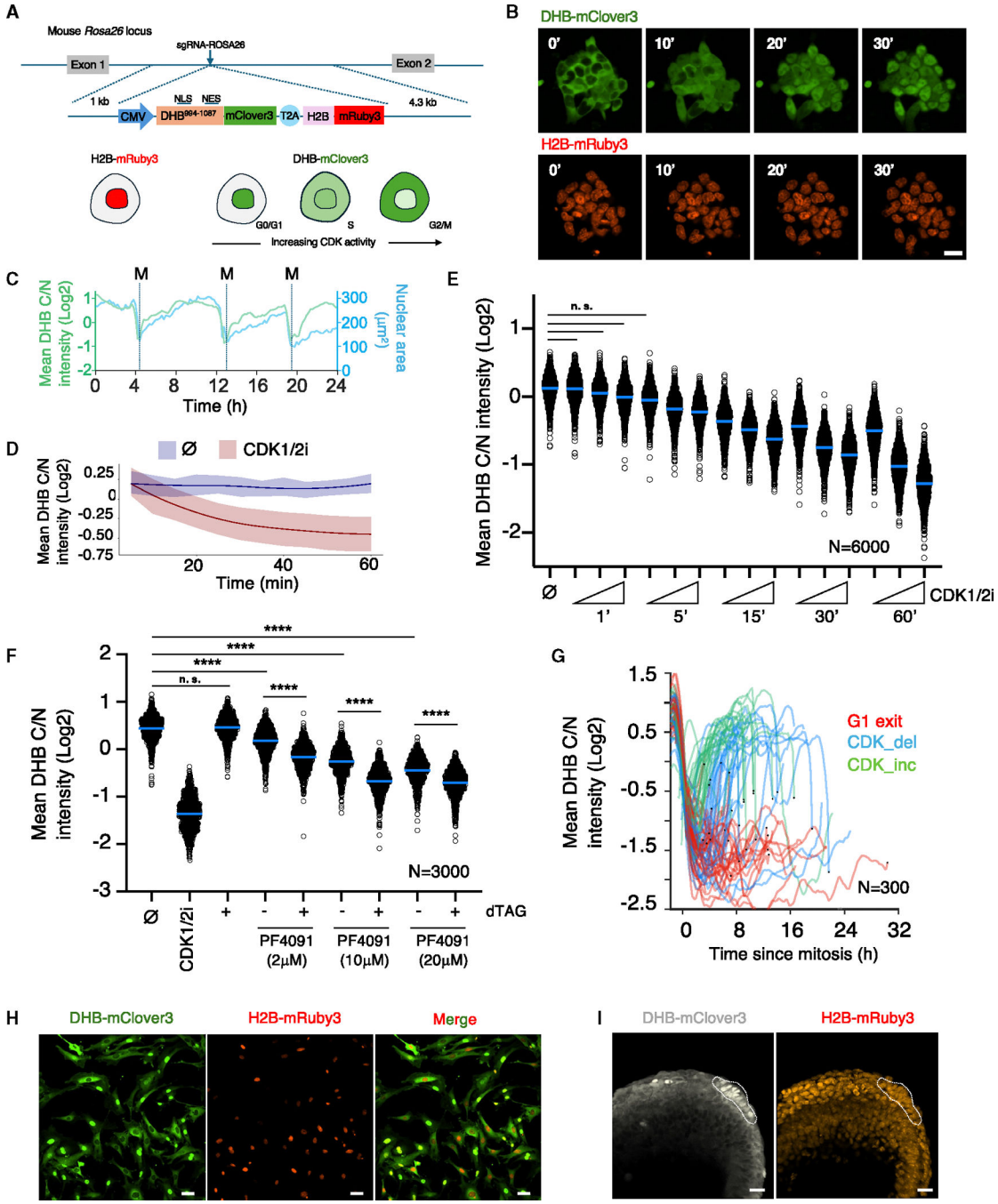

Figure 1. A mouse model to visualize CDK activity

(A) CDK sensor targeted at the *Rosa26* locus. NES, nuclear export signal; NLS, nuclear localization signal.

(B) Confocal images of mouse ESC$^{DHB/H2B}$ treated with CDK1/2i (30 μM). Scale bar, 30 μm.

(C) Single-cell CDK activity (green) and nuclear size (blue) traces of representative ESC$^{DHB/H2B}$. We tracked the same cell and followed a daughter and granddaughter cell after mitosis (M).

(D) Plot showing mean CDK activity with a shading of minimum and maximum values in untreated (ø) or CDK1/2i-treated (30 mM) $ESC^{DHB/H2B}$.

(E) High-throughput imaging (HTI) quantification of CDK activity in untreated (ø) or CDK1/2i-treated $ESC^{DHB/H2B}$ cultures at different time points and concentrations (1, 5, and 30 μM). Center lines indicate mean values. All comparisons to untreated cells showed $p < 0.0001$ from two-tailed unpaired t tests. n.s., non-significant.

(F) HTI quantification of CDK activity in untreated (ø) or dTAG-treated CDK1-degron $ESC^{DHB/H2B}$ combined with PF4091 for 2 h. Center lines indicate mean values. *p* values are from two-tailed unpaired t tests. ****$p < 0.0001$.

(G) Single-cell CDK activity traces from $ROSA26^{DHB/H2B}$-derived MEFs. All tracks were synchronized *in silico* to mitosis. Criteria to define cells as CDK_inc, CDK_del, and G1 exit are specified in STAR Methods.

(H) Confocal images of untreated $ROSA26^{DHB/H2B}$-derived MEFs. Scale bar, 50 μm.

(I) Confocal images of E7.5 $ROSA26^{DHB/H2B}$ mice showing the node (dashed lines). Scale bar, 20 μm.

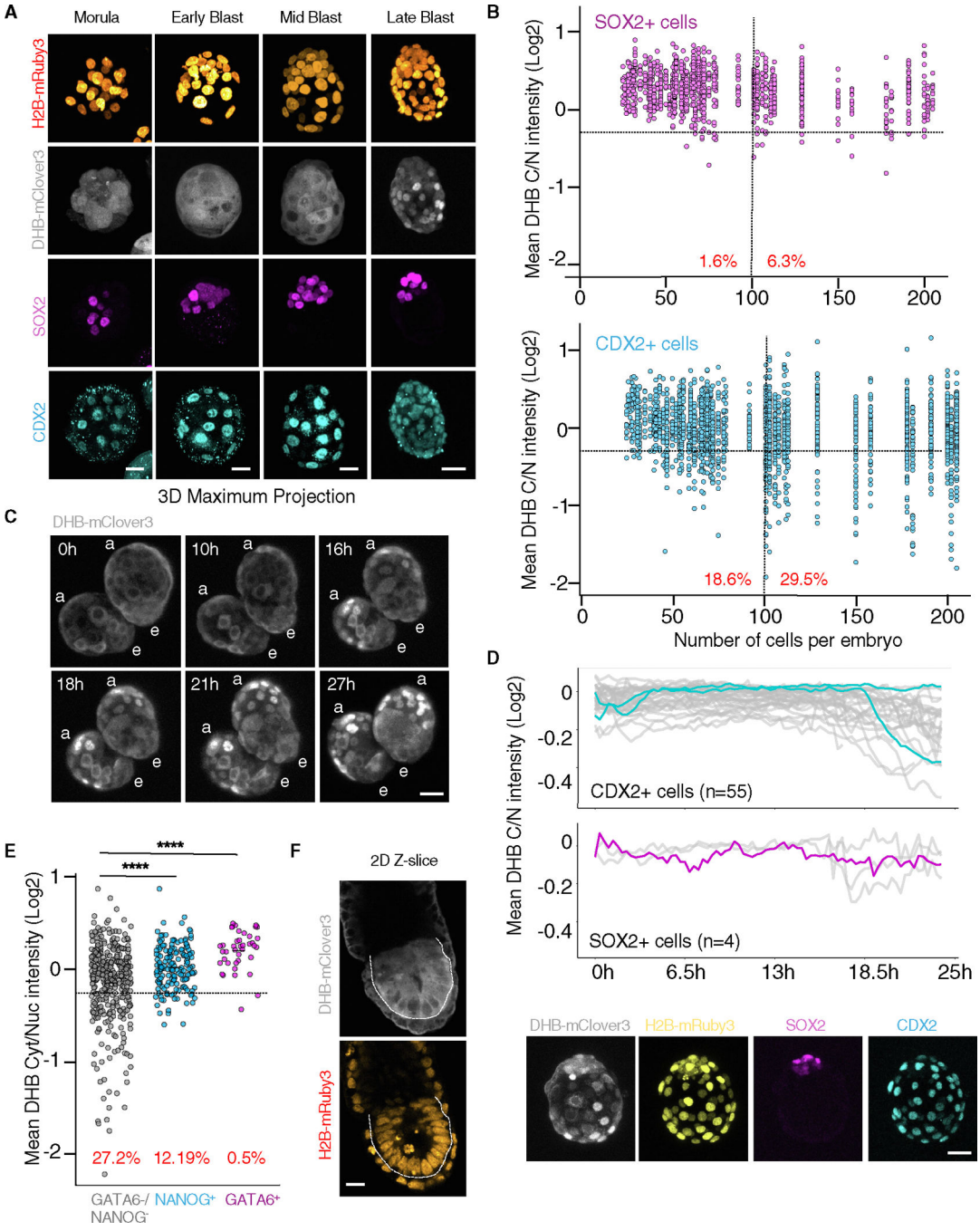

Figure 2. TE cells show decreased CDK activity upon implantation

(A) Confocal images from representative ROSA26$^{DHB/H2B}$ embryos. Scale bar, 20 μm.

(B) Plot showing a quantification of CDK activity in individual SOX2^{+} or CDX2^{+} cells from ROSA26$^{DHB/H2B}$ embryos (dots from the same column) staged based on the number of cells. Percentage of cells (in red) below the arbitrary threshold (−0.25) shown for embryos containing 0–100 cells and above 100 cells. N = 54 embryos.

(C) Time-lapse microscopy experiment performed in two representative E3.5 ROSA26$^{DHB/H2B}$ embryos. Note the embryonic (e)-abembryonic (a) axis. Scale bar, 30 μm.

(D) Plots showing CDK activity in individual cells obtained from a representative E3.5 ROSA26$^{DHB/H2B}$ embryo. The embryo was imaged, fixed, and stained for CDX2 and SOX2 (bottom; scale bar, 30 μm) to determine lineage identity at the endpoint. Highlighted tracks are in cyan and magenta.

(E) Plot showing a quantification of CDK activity in individual cells obtained from a pool of E4.5 ROSA26$^{DHB/H2B}$ embryos. Percentage of cells (in red) below the arbitrary threshold (−0.25). p values are from two-tailed unpaired t tests. ****$p < 0.0001$; $N = 5$ embryos.

(F) Confocal images from E6.5 ROSA26$^{DHB/H2B}$ embryos. Dashed line surrounds the EPI. Scale bar, 20 μm.

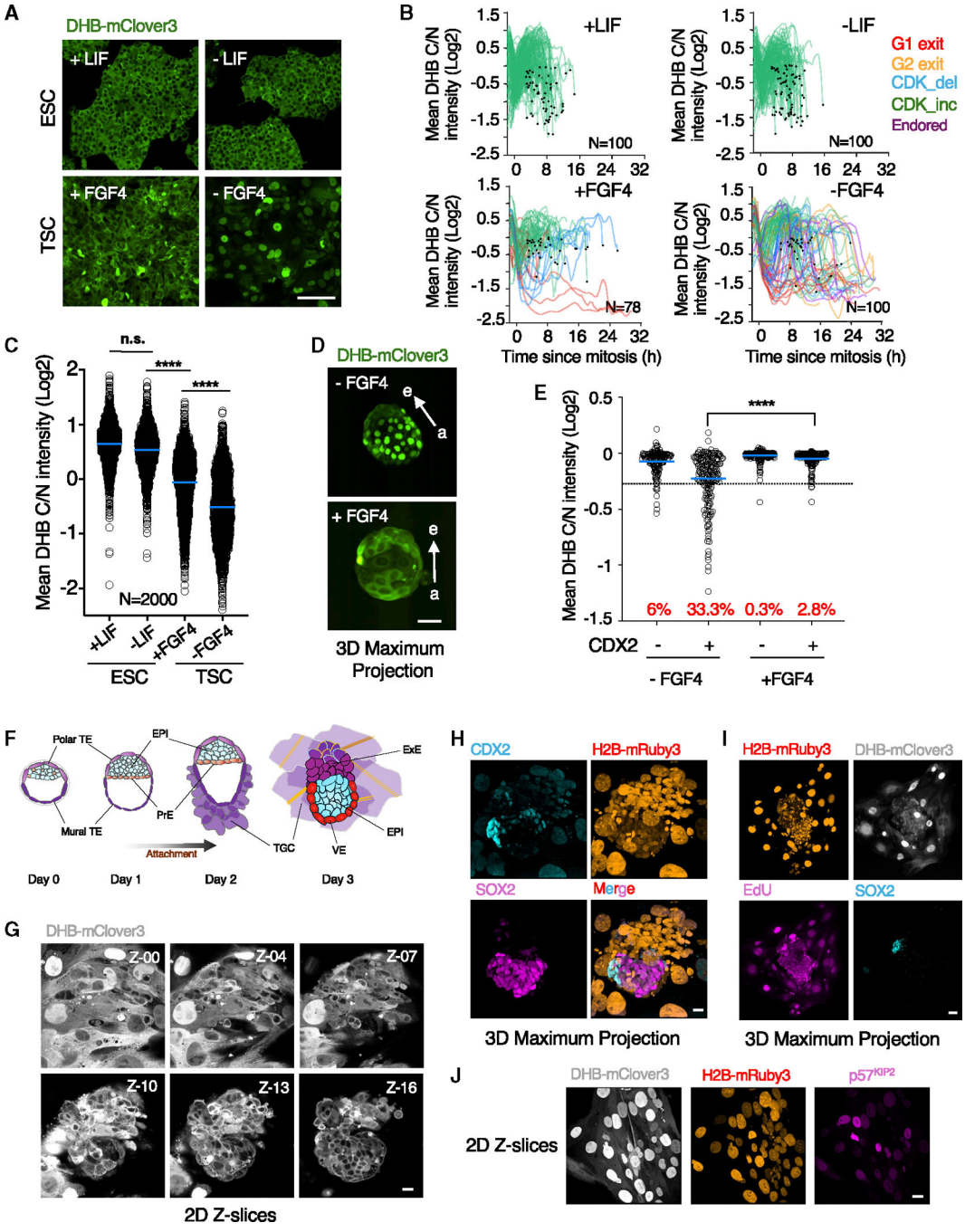

Figure 3. ICM-derived FGF4 establishes a CDK activity gradient

(A and B) Confocal images (A; scale bar, 100 μm) and single-cell CDK activity traces (B) from $TSC^{DHB/H2B}$ and $ESC^{DHB/H2B}$ cultured with or without self-renewal signals for 72 h. In (B), all tracks were synchronized *in silico* to mitosis. Criteria to define cells as CDK_inc, CDK_del, Endored, G1 exit and G2 exit are specified in STAR Methods.

(C) HTI quantification of CDK activity in $ESC^{DHB/H2B}$ and $TSC^{DHB/H2B}$ under self-renewal conditions or following self-renewal factor withdrawal for 72 h. Center lines indicate mean values. ****$p < 0.0001$ from two-tailed unpaired t tests.

(D) Confocal images of representative E3.5 untreated or FGF4-treated ROSA26$^{DHB/H2B}$ embryos cultured for 20 h. Scale bar, 50 μm. Arrows indicate the embryonic (e)-abembryonic (a) axis.

(E) Plot showing CDK activity levels in a pool of CDX2^{+} or CDX2^{-} cells from untreated (N = 5 embryos) or FGF4-treated (N = 9 embryos). p value is from a two-tailed unpaired t test. ****$p < 0.0001$. In red is the percentage of cells below the arbitrary threshold (−0.25).

(F) Schematic representation of the development of a E3.5 blastocyst (day 0 for *in vitro* culture) beyond implantation stages.

(G–J) Series of 2DZ-slices obtained from a Z-stack (G and J) or maximum projection (H and I) confocal images of representative ROSA26$^{DHB/H2B}$ embryos cultured *in vitro* 3 days after isolation at E3.5. Scale bars, 20 μm (G and H), 50 μm (I), and 30 μm (J).

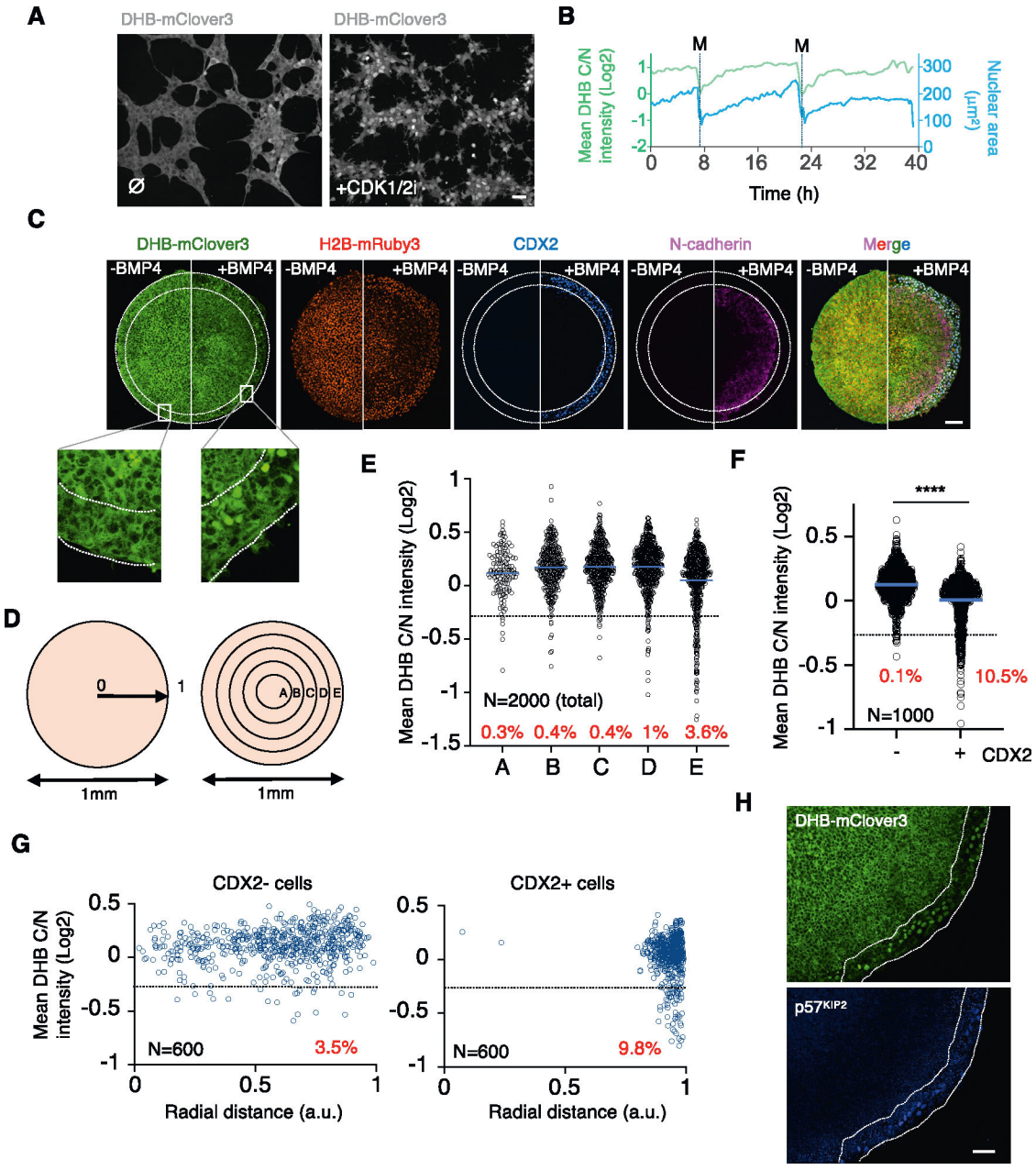

Figure 4. Human TE-like cells show nuclear translocation of the CDK sensor

(A) Confocal images of human ESC$^{DHB/H2B}$ untreated (ø) or CDK1/2i-treated (30 μM) for 1 h. Scale bar, 50 μm.

(B) Single-cell CDK activity and nuclear trace of representative human ESC$^{DHB/H2B}$.

(C) Confocal images of uninduced or BMP4-induced gastruloids. Insets show higher magnification. Dashed lines highlight TE-like cells. Scale bar, 100 μm.

(D) Representation of the gastruloid using radial distance (left) or concentric rings (right).

(E–G) Plot showing CDK activity levels in 2,000 random cells distributed according to their position (E), 1,000 random CDX2^{+} or CDX2^{-} cells (F), and 600 random CDX2^{+}/CDX2^{-} cells according to their radial distance (G). Percentage of cells per ring (in red) below the

arbitrary threshold (<−0.25). Data obtained by combining multiple gastruloids ($N = 12$). p value is from a two-tailed unpaired t test. ****$p < 0.0001$.
(H) Confocal images of representative BMP4-induced gastruloids. Dashed lines highlight TE-like cells. Scale bar, 50 μm.

KEY RESOURCES TABLE

REAGENT or RESOURCE	SOURCE	IDENTIFIER
Antibodies		
Mouse Anti-CDX2	BioGenex	MU392A-UC, RRID:AB_2923402
Rabbit Anti CDX2	Abcam	ab76541, RRID:AB_1523334
Mouse Anti $p57^{KIP2}$	Santa Cruz	sc-56341, RRID:AB_785045
Mouse Anti TFAP2C	Santa Cruz	sc-12762, RRID:AB_667770
Rabbit Anti Brachyury	Abcam	ab209665, RRID:AB_2750925
Rabbit Anti Sox2	Cell Signaling	23064S, RRID:AB_2714146
Rabbit Anti Phospho-CDK substrate Motif	Cell Signaling	9477, RRID:AB_2714143
Goat Anti Gata6	R&D systems	AF1700, RRID:AB_2108901
Rabbit Anti Nanog	Abcam	ab80892, RRID:AB_2150114
Mouse Anti N-Cadherin	Cell Signaling	#14215, RRID:AB_2798427
Rabbit Anti Phospho-SMAD1/5	Cell Signaling	#9516, RRID:AB_491015
Rabbit Anti CDK1	Millipore	06–923, RRID:AB_11214395
Chemicals, peptides, and recombinant proteins		
CDK1/2 inhibitor	Sigma-Aldrich	217714
CDK2 inhibitor (PF-07104091)	Axon MEDCHEM	3753
CDK1 inhibitor (Ro3306)	Sigma-Aldrich	SML0569
Palbociclib (PD-0332991)	Selleckchem	S1116
Recombinant Human FGF4	R&D Systems	235-F4-025
Heparin	Sigma-Aldrich	H3149-10KU
M2	EMD Millipore	MR-015-D
EmbryoMax KSOM	EMD Millipore	MR-106-D
Silicon oil	Chem-Cruz	sc-215854
GoTaq® Hot Start Polymerase	Promega	M500B
Proteinase K	Meridian Bioscience	BIO-37084
Paraformaldehide (PFA)	EMS	15710
Acid Tyrode’s	Sigma-Aldrich	T1788
Glycine	Sigma-Aldrich	50046-250G
Triton X-100	Sigma-Aldrich	T8787
DMEM	Gibco	11965–092
DMEM-F12	Gibco	11320–033
RPMI	Quality Biological	112-025-101
NEAA	Gibco	11140–050
Glutamax	Gibco	35050–61
Sodium Pyruvate	Gibco	11360–070
2-mercaptoethanol	Gibco	31350–010
Fetal Bovine Serum	GEMINI Bio products	100–525
0.05% Trypsin EDTA	Gibco	25300–054
Gelatin	Sigma-Aldrich	G1890

REAGENT or RESOURCE	SOURCE	IDENTIFIER
Penicillin/Streptomycin	Gibco	15070–063
mTeSR PLUS	Stem Cell Technologies	100–0276
RSeT™ Medium	Stem Cell Technologies	05978
Dispase	Stem Cell Technologies	7923
Accutase	Gibco	A11105-01
Matrigel Growth Factor Reduced	Corning	3566231
Rho kinase inhibitor, Y27632	Selleckchem	S1049
BMP4	R&D Systems	314-BP-010
Laminin	BioLamina	LN521-04
ITS-X	Life Technologies	51500–056
β-Estradiol	Sigma-Aldrich	E8875
Progesterone	Sigma-Aldrich	P0130
N-Acetyl-L-cysteine	Sigma-Aldrich	A7250
Pregnant Mare Serum Gonadotropin	PROSPEC	hor-272
Chorionic Gonadotropin Human	PROSPEC	hor-250
Bovine Serum Albumin (BSA)	Sigma-Aldrich	3117332001
Tween 20	Sigma-Aldrich	9005-64-5
Experimental models: Cell lines		
HEK293T	Inder Verma, Salk Institute	Gift
R1 ESC	Sagrario Ortega, CNIO	Gift
R1 ESC ROSA26$^{DHB/DHB}$	N/A	This paper
R1 ESC ROSA26$^{DHB/DHB}$; CDK2^{kO}	N/A	This paper
R1 ESC ROSA26$^{DHB/DHB}$; CDK1^{FKBP}	N/A	This paper
MEF ROSA26$^{DHB/DHB}$	N/A	This paper
WA09	WiCell	WB68075
WA09-(H9)$^{DHB/DHB}$	WiCell	This paper
WA09-(H9)$^{DHB/DHB}$; CDK2^{KO}	WiCell	This paper
Trophoblast stem cells (TSC)	Magdalen Zernicka-Goetz, Caltech	Gift
TSC$^{DHB/DHB}$	N/A	This paper
Deposited Data		
Code used for imaging analysis	Zenodo	10.5281/zenodo.14230496 (https://zenodo.Org/records/14230496)
Experimental models: Organisms/strains		
C57BL/6J	The Jackson Laboratory	000664
C57BL/6J-ROSA26$^{DHB/DHB}$	N/A	This paper
Oligonucleotides		
Primers for qRT-PCR, see table 1	N/A	N/A
Primers for sgRNA, see table 1	N/A	N/A

REAGENT or RESOURCE	SOURCE	IDENTIFIER
Recombinant DNA		
LSL-Cas9-ROSA26TV	Addgene	#61408
ROSA26TV-DHB-Clover3_2A_H2B-RFP (recombination construct)	N/A	This paper
FUGW	Addgene	#14883
FUGW-DHB-Clover3_2A_H2B-RFP	N/A	This paper
LentiCRISPRv2	Addgene	#52961
mAC-CDK1-2xHA-FKBP-2A-TagBFP (recombination construct)	N/A	This paper
Software and algorithms		
Imaris	Oxford Instruments	RRID:SCR_007370
Arivis	Zeiss	RRID:SCR_018000
ImageJ	Schneider et al., 2012	RRID:SCR_003070
NIS-Elements	Nikon	RRID:SCR_014329
R Studio 2024.04.1 +748	Posit Software	RRID:SCR_000432
Signals Image Artist	Revvity Signals Software, Inc.	https://revvitysignals.com/
Python (v. 3.10)		RRID:SCR_008394
Other		
μ-Slide 18 well ibiTreat	Ibidi	#81811
μ-Slide 18 well uncoated	Ibidi	#81811
μ-Slide 8 well ibiTreat	Ibidi	#80821